Equatorial Pacific pCO_2 Interannual Variability in CMIP6 Models

Suki C. K. Wong[1], Galen A. McKinley[1], Richard Seager[1]

[1]Lamont-Doherty Earth Observatory, Columbia University, Palisades, New York

Key Points:

- The majority of models underestimate pCO_2 IAV, while they overestimate SST IAV
- Competing thermal and non-thermal pCO_2 components are not appropriately balanced in models, which results in weak total pCO_2 IAV
- Vertical DIC gradients are biased weak more than temperature gradients, but this alone doesn't explain the relative sizes of pCO_2 components

Corresponding author: Suki Wong, `suki.wong@columbia.edu`

Abstract

The El Niño-Southern Oscillation (ENSO) in the equatorial Pacific is the dominant mode of global air-sea CO_2 flux interannual variability (IAV). Air-sea CO_2 fluxes are driven by the difference between atmospheric and surface ocean pCO_2, with variability of the latter driving flux variability. Previous studies found that models in Coupled Model Intercomparison Project Phase 5 (CMIP5) failed to reproduce the observed ENSO-related pattern of CO_2 fluxes and had weak pCO_2 IAV, which were explained by both weak upwelling IAV and weak mean vertical DIC gradients. We assess whether the latest generation of CMIP6 models can reproduce equatorial Pacific pCO_2 IAV by validating models against observations-based data products. We decompose pCO_2 IAV into thermally and non-thermally driven anomalies to examine the balance between these competing anomalies, which explain the total pCO_2 IAV. The majority of CMIP6 models underestimate pCO_2 IAV, while they overestimate SST IAV. Thermal and non-thermal pCO_2 anomalies are not appropriately balanced in models, such that the resulting pCO_2 IAV is too weak. We compare the relative strengths of the vertical transport of temperature and DIC and evaluate their contributions to thermal and non-thermal pCO_2 anomalies. Model-to-observations-based product comparisons reveal that modeled mean vertical DIC gradients are biased weak relative to their mean vertical temperature gradients, but upwelling acting on these gradients is insufficient to explain the relative magnitudes of thermal and non-thermal pCO_2 anomalies.

Plain Language Summary

To date, the global ocean has been responsible for absorbing over a third of carbon dioxide (CO_2) emissions, slowing down the growth of atmospheric CO_2 levels which drives global warming. Of interest is the equatorial Pacific Ocean, which is the largest oceanic source of CO_2 to the atmosphere with large fluctuations that are apparent in the record of global atmospheric CO_2. To study the ocean's ability to absorb future CO_2 emissions, we need models of the Earth system that can accurately capture fluctuations in the equatorial Pacific. In this paper, we assess surface ocean CO_2 fluctuations in the equatorial Pacific in the latest generation of models and we examine their deviations from observations. Compared to observations, models underestimate surface ocean CO_2 fluctuations as a result of excessive cancellation between competing drivers of CO_2 change. We find that the vertical gradient of carbon in models is too weak, which through ocean circulation, would contribute to weak surface CO_2 fluctuations. However, this does not fully account for underestimations in surface CO_2 fluctuations. Other processes have a significant role in excessively canceling surface CO_2 concentrations and requires further research.

1 Introduction

Carbon dioxide (CO_2) in the atmosphere is the main driver of anthropogenic radiative forcing via the greenhouse effect. Natural sinks in the ocean and land are damping the atmospheric CO_2 growth rate. The latest assessment of the global carbon budget averaged over recent decades (1960-2020) estimates the airborne fraction of atmospheric CO_2 emissions to be about 45%, with the remainder of emissions partitioned among the ocean (25%) and land (30%) (Friedlingstein et al., 2022). However, uncertainties in quantifying aspects of the global carbon cycle result in an imbalance in the carbon budget, which is largely attributed to errors in land and ocean sink estimates (Friedlingstein et al., 2022). Constraining ocean interannual variability (IAV) will help to reduce uncertainty in land IAV.

The equatorial Pacific is the largest natural oceanic source of CO_2 to the atmosphere (Takahashi et al., 2009), as a result of wind-driven upwelling in the region; upwelling brings cool waters that are rich in dissolved inorganic carbon (DIC) to the surface, which in-

creases the partial pressure of CO_2 in the surface ocean (pCO_2). CO_2 outgassing IAV in the equatorial Pacific is dominated by the El Niño-Southern Oscillation (ENSO), and is the dominant mode of global ocean sink IAV (Rödenbeck et al., 2014). ENSO mechanisms of air-sea CO_2 flux (FCO_2) variability are well understood. During an ENSO warm phase (El Niño), slackening trade winds over the equator reduces upwelling and brings about warm sea surface temperature (SST) anomalies (Bjerknes, 1966). Warm SST anomalies increase pCO_2 via reduced CO_2 solubility. However, it is the reduction in surface DIC due to reduced upwelling that dominates the CO_2 response (reduced CO_2 outgassing) during an El Niño (McKinley et al., 2004). During an ENSO cold phase (La Niña), the opposite happens and CO_2 outgassing is enhanced.

In Coupled Model Intercomparison Project Phase 5 (CMIP5), atmosphere-ocean global climate models were coupled with biogeochemical processes for the first time in CMIP history, allowing for carbon cycling in models (Taylor et al., 2012; Emori et al., 2016). Studies have reported biases in simulated equatorial Pacific pCO_2 and FCO_2 IAV in CMIP5 models, where weak surface DIC variability was found to be a source of bias in some models (Dong et al., 2017; Jin et al., 2019). Given ongoing climate change, there is a need for Earth System Models (ESMs) to make accurate climate projections. The latest generation of ESMs from CMIP6 have demonstrated progress in representing the mean state of ocean biogeochemistry (Séférian et al., 2020). However, as in CMIP5, weak FCO_2 IAV were also found in CMIP6 (Vaittinada Ayar et al., 2022). Identifying sources of model biases in FCO_2 IAV for the contemporary period, where some data constraints exist, is a first step towards model improvements.

Here, we assess equatorial Pacific pCO_2 IAV in 18 CMIP6 models over recent decades, comparing amplitudes and spatial patterns of variability against state-of-the-art observations-based pCO_2 products that span over five decades. We also compare the covariability of ENSO-related variables, such as SSTs, vertical velocity at 50m (w_{50}), and thermocline depths with pCO_2 anomalies across the CMIP6 subset through lagged correlations. To understand biases in pCO_2 IAV, we decompose pCO_2 IAV into thermally (SST) and non-thermally (DIC, alkalinity and salinity) driven components. Imbalances between these competing components provide insight on biases in the total pCO_2 IAV.

In the equatorial Pacific, surface DIC variability dominates pCO_2 variability (Doney et al., 2009). Though there are several processes that drive DIC variability (FCO_2, freshwater fluxes, biology, vertical and horizontal transport), studies show that variability in the vertical transport of DIC is important to the overall budget of pCO_2 variability in the equatorial Pacific Ocean (Liao et al., 2020). Including temperature-driven pCO_2 variability, Liao et al. (2020) showed that the vertical transport term contributed the largest amount in their full mixed-layer pCO_2 budget decomposition (accounting for about 40% of the pCO_2 response; FCO_2 $\sim$ 20%; biology $\sim$ 18%; freshwater fluxes $\sim$ 11%; horizontal transport $\sim$ 10%; thermal and residual $<$ 1%). This demonstrated importance of the vertical transport of DIC in the equatorial Pacific motivates our investigation of its variability in CMIP6. There is also reason to believe that models are biased in mean vertical gradients (Li & Xie, 2012; Farneti et al., 2022), which through upwelling, could contribute to biases in surface DIC variability.

Our objectives are as follows: 1) compare equatorial Pacific pCO_2 IAV in CMIP6 models against observations-based data products, 2) understand why models underestimate pCO_2 IAV, and 3) identify sources of bias in the vertical transport of DIC in models. Given biases in mean vertical gradients of DIC and temperature, we quantify the degree to which upwelling anomalies (acting on biased gradients) contribute to the relative magnitudes of non-thermal and thermal pCO_2 IAV, respectively. Such assessment is necessary to ground work on how future changes in the variability and mean state of the tropical Pacific atmosphere-ocean system will also impact variability and shifts in air-sea CO_2 fluxes, with potential climate impact.

Table 1. The CMIP6 models in this assessment and their references. For information about the ensemble members, see Table S1. Models in bold have a correct sign correlation between pCO_2 and vertical velocity and are assessed in all parts of this study.

Models	Reference
ACCESS-ESM1-5	(Ziehn et al., 2019)
CanESM5	(Swart et al., 2019b)
CanESM5-CanOE	(Swart et al., 2019a)
CESM2	(Danabasoglu, 2019b)
CESM2-FV2	(Danabasoglu, 2019a)
CESM2-WACCM	(Danabasoglu, 2019d)
CESM2-WACCM-FV2	(Danabasoglu, 2019c)
CNRM-ESM2-1	(Seferian, 2018)
GFDL-CM4	(Guo et al., 2018)
IPSL-CM6A-LR	(Boucher et al., 2021)
MIROC-ES2L	(Hajima et al., 2019)
MRI-ESM2-0	(Yukimoto et al., 2019)
MPI-ESM1-2-LR	(Wieners et al., 2019)
MPI-ESM1-2-HR	(Jungclaus et al., 2019)
MPI-ESM-1-2-HAM	(Neubauer et al., 2019)
NorESM2-LM	(Seland et al., 2019)
NorESM2-MM	(Bentsen et al., 2019)
UKESM1-0-LL	(Byun, 2020)

2 Models, Data and Methods

2.1 Models

Outputs from historical simulations (1959-2014) from 18 CMIP6 models (Table 1) are from the Pangeo cloud (`http://pangeo.io`), which were originally downloaded from the Earth System Grid Federation's online archives (`http://esgf-node.llnl.gov/projects/cmip6`). We apply a data pre-processing Python tool to clean and unify data inconsistencies before any analysis (Busecke & Abernathey, 2020). We assess 18 models which have monthly pCO_2, FCO_2, SST, near-surface wind speeds measured at 10m (u_{10}), ocean temperatures (T), w_{50} and DIC data available. Vertical velocities are calculated using the three-dimensional continuity equation for models that only have horizontal circulation data. For analyses that involve multiple ensemble members, ensemble members are chosen only if they have outputs for all the variables named above. This ensures that the internal variability, unique to each run of a model (an ensemble member), is conserved across all output variables from a single run. For a list of the members that we use for each model, see Table S1.

2.2 Observations-based Data Products

We use five out of the six available monthly gridded observations-based pCO_2 products from SeaFlux (Fay et al., 2021) for FCO_2 and surface ocean pCO_2 estimates. These five products include JENA-MLS, MPI-SOMFFN, CMEMS-FFN, JMA-MLR and CSIR-ML6. We exclude a sixth product (NIES-FFNN) from our assessment as it was not able to recreate ENSO variability in pCO_2, such as the strong 1997-98 El Niño event seen in the other products. For u_{10} data, we also use the three wind reanalysis products (CCMPv2, JRA55 and ERA5), used in SeaFlux to estimate fluxes.

DIC and total alkalinity (Alk) climatologies are from GLODAPv2 (Lauvset et al., 2021). GLODAPv2 is a mapped three-dimensional climatological data product of inorganic and carbon-related ocean variables. Observations of DIC and Alk are distributed in time too scarcely to allow determination of its time variation, so in GLODAPv2, the data have been averaged into a DIC climatology estimate. Monthly estimates of SST, ocean circulation and ocean temperature (1959-2014) are from a reanalysis product, ORAS5 of the European Center for Medium Range Weather Forecasts (Zuo et al., 2019). Unlike DIC and Alk, time variations can be resolved for SST, ocean circulation and ocean temperature variables in observations-based data products. We calculate vertical velocity using zonal and meridional ocean circulation data from ORAS5 via the vertical integration of the continuity equation. SST observations from another dataset, HadISST (1959-2014; Rayner et al. (2003)), are a secondary source for SST comparisons against models.

2.3 Methods

Model outputs are regridded to the same $1°\times1°$ longitude-latitude grid before any analysis. We define a region of the equatorial Pacific (5°N-5°S) between 180°E and 270°E, which encompasses the Niño 3 and 3.4 regions, extending 10 degrees west of Niño 3.4, and refer to it as the Tropical Pacific Index (TPI) region. The Niño 3 and 3.4 regions are typically used to study the nature of ENSO variability over the equatorial Pacific Ocean, but here, the broader TPI region was chosen such that any longitudinal differences in the ENSO centers of action in models would be captured.

To compare relative amplitudes of IAV across models and other datasets, we use one standard deviation (σ) of detrended and deseasonalized monthly anomalies. Modeled FCO_2, pCO_2 and u_{10} IAV are compared against SeaFlux IAV. Note that historical simulations in CMIP6 models generate their own internal climate variability, and will not replicate the timings of historical events unless they are externally forced. Thus, when comparing SeaFlux IAV to model IAV, the temporal evolution is not expected to match. When calculating and comparing multi-year means between CMIP6 models and SeaFlux, data from the same time frame (1990 to 2014) are compared. This is done since multi-year means are sensitive to anthropogenic trends in CO_2; the ocean sink is changing over time in both observations-based data products and historical simulations, such that multi-year means are sensitive to the time frame over which the average is taken. The 1990-2014 time frame is chosen for multi-year means, because temporal coverage begins in 1990 for SeaFlux, and 2014 is the end year for CMIP6 historical simulations. Climatological monthly means taken over the study period are subtracted from monthly timeseries data to obtain deseasonalized monthly anomalies, and then, the data are detrended with the least squares method. In addition to model comparisons against SeaFlux, modeled SST IAV and vertical DIC gradients IAV are also compared against observations-based data products.

Spatial patterns of pCO_2 IAV are compared and assessed by calculating its first empirical orthogonal function (EOF) after detrending and deseasonalizing. EOF analyses are done on individual ensemble members that retain full internal variability, and then averaged across ensemble members. The first principal components (PC1) and associated EOFs are all shown for the La Niña state, as determined with reference to the sign of the TPI SST index. Model performances in reproducing IAV are assessed using spatial correlation coefficients (SCC) between each model and observations-based pCO_2 patterns of IAV.

In order to examine the mechanisms of pCO_2 variability in models, local correlations between pCO_2 and SST anomalies within the tropical Pacific are calculated. Areas of strong correlations indicate regions in models where upwelling dominates pCO_2, which is consistent with the dominant ENSO signal. Lagged temporal correlations be-

tween pCO_2, SST, w_{50} and thermocline depth (z_{therm}) anomalies are also done to investigate the covariability of ENSO-related variables to pCO_2 anomalies. We define the z_{therm} as the depth of the maximum vertical temperature gradient. Time lags between variables are based on the lags seen in the observations-based data products: pCO_2 and SST are concurrently correlated, while w_{50} and z_{therm} anomalies lead pCO_2 by up to 3 months. Three-month running means of w_{50} and z_{therm} anomalies are taken before correlating them to the pCO_2 of the fourth month (e.g., the January-to-March mean of w_{50} anomalies are correlated to April's pCO_2 anomaly). pCO_2 is long-lived in the ocean, such that the influence of w_{50} and z_{therm} variability on local pCO_2 advects west due to mean currents during the three months of lag. To account for some of the westward advection of pCO_2 during the lag period, w_{50} and z_{therm} anomalies are calculated over a region 20° east of the TPI box region before correlating with pCO_2 anomalies over the TPI box region.

2.4 Thermal and Non-thermal pCO_2 IAV

Variability in DIC, alkalinity (Alk) and salinity (S) are the non-thermal drivers of pCO_2 variability, while SST variability is the thermal driver. Thermal effects on pCO_2 typically oppose and dampen the non-thermal effects with ENSO (Sutton et al., 2014): for example, a reduction in upwelling brings less DIC to the surface which decreases surface pCO_2; simultaneously, the warmer SST anomalies, as a result of weakened upwelling, drives surface pCO_2 up via reduced solubility. We separate the non-thermally driven pCO_2 ($pCO_{2,nonT}$) from the thermally-driven counterpart ($pCO_{2,T}$) in order to explain modeled pCO_2 IAV. For $pCO_{2,nonT}$, temperature effects are removed by normalizing pCO_2 outputs to a long-term mean SST (Takahashi et al., 2002), following an empirical formulation determined by Takahashi et al. (1993):

$$pCO_{2,nonT} = pCO_2 \times \mathrm{e}^{0.0423\cdot(\overline{\mathrm{SST}}-\mathrm{SST})}, \tag{1}$$

where $\overline{\mathrm{SST}}$ is the multiyear mean of SST over time. The thermally driven component, $pCO_{2,T}$, is computed using the following equation (Takahashi et al., 2002):

$$pCO_{2,T} = \overline{pCO_2} \times \mathrm{e}^{0.0423\cdot(\mathrm{SST}-\overline{\mathrm{SST}})}, \tag{2}$$

where $\overline{pCO_2}$ is the multiyear mean of pCO_2 during 1990-2014.

2.5 Vertical Transport of DIC

Temporal changes in pCO_2 are a function of temporal changes in DIC, Alk, S and T, and can be expressed as the following linearly decomposed time derivative (Takahashi et al., 1993; Le Quéré et al., 2000; Liao et al., 2020):

$$\partial_t pCO_2 = \underbrace{\frac{\partial pCO_2}{\partial \mathrm{DIC}}\partial_t \mathrm{DIC} + \frac{\partial pCO_2}{\partial \mathrm{Alk}}\partial_t \mathrm{Alk} + \frac{\partial pCO_2}{\partial \mathrm{S}}\partial_t \mathrm{S}}_{\mathrm{non-thermal}} + \underbrace{\frac{\partial pCO_2}{\partial \mathrm{T}}\partial_t \mathrm{T}}_{\mathrm{thermal}}, \tag{3}$$

where we use the notation ∂_t to denote a partial derivative with respect to time. Temporal changes in DIC, Alk and S drive $pCO_{2,nonT}$, while temporal changes in SST drive $pCO_{2,T}$.

In the tropical Pacific, DIC variability has been found to be the dominant driver of pCO_2 variability, compared to Alk, S and T drivers (Doney et al., 2009; Le Quéré et al., 2000). Note that Liao et al. (2020) found that in some cases, alkalinity-driven effects on pCO_2 can exceed DIC-driven effects, though DIC effects generally dominate in the equatorial Pacific. Other model studies confirm that DIC is the dominant term in the region (Jin et al., 2019; Long et al., 2013).

The time tendency of surface DIC (∂_tDIC) is controlled by several processes including horizontal and vertical ocean transport, FCO_2, biological processes and freshwater fluxes:

$$\partial_t \mathrm{DIC} \approx \partial_t \mathrm{DIC_H} + \partial_t \mathrm{DIC_V} + \partial_t \mathrm{DIC_{FCO_2}} + \partial_t \mathrm{DIC_{Bio}} + \partial_t \mathrm{DIC_{FW}} \tag{4}$$

In this study, we assess only the variability in vertical transport of DIC ($\partial_t \mathrm{DIC}_V$). Liao et al. (2020) showed that though other processes are non-negligible, vertical transport contributed the largest effect on pCO_2 change. They also showed that the other processes are sensitive to changes in vertical transport: an increase in upwelling (increased surface DIC) drives an air-sea flux response, which damps surface DIC; upwelled nutrient-rich waters increase biological activity causing an increased uptake of DIC, which again damps surface DIC; and the horizontal transport of increased surface DIC results in a diverging transport, also damping.

In order to quantify the contribution of the vertical transport of DIC ($\partial_t \mathrm{DIC}_V$) to $pCO_{2,nonT}$ variability ($\partial_t pCO_{2,nonT}$), we evaluate the former in the same units as the latter - in units of the time tendency of pCO_2 (μatms^{-1}) - and write $\partial_t \mathrm{DIC}_V$ as $w_{50}\partial_z$DIC. Using coefficients from Equation 3, we can get both terms into the same units:

$$\frac{\partial pCO_2}{\partial \mathrm{DIC}} w_{50} \partial_z \mathrm{DIC} \quad [\text{units} : \mu\text{atm } s^{-1}] \tag{5}$$

$$\partial_t pCO_{2,nonT} \quad [\text{units} : \mu\text{atm } s^{-1}] \tag{6}$$

The coefficients used for the pCO_2 dependence on DIC are approximated as follows (Lovenduski et al., 2007):

$$\frac{\partial pCO_2}{\partial \mathrm{DIC}} \approx \frac{\overline{pCO_2}}{\overline{\mathrm{DIC}}} \cdot \frac{3 \times \overline{\mathrm{Alk}} \times \overline{\mathrm{DIC}} - 2 \times \overline{\mathrm{DIC}}^2}{(2 \times \overline{\mathrm{DIC}} - \overline{\mathrm{Alk}})(\overline{\mathrm{Alk}} - \overline{\mathrm{DIC}})}, \tag{7}$$

which can be expressed more simply as:

$$\frac{\partial pCO_2}{\partial \mathrm{DIC}} \approx \frac{\overline{pCO_2}}{\overline{\mathrm{DIC}}} \cdot \gamma_{\mathrm{DIC}}, \tag{8}$$

where γ_{DIC} is the buffer factor (Sarmiento & Gruber, 2006).

2.6 Reynolds' Decomposition

Using Reynolds' decomposition, we can separate the mean and the time-varying component:

$$w_{50} = \overline{w_{50}} + w'_{50}, \text{and} \tag{9}$$

$$\partial_z \mathrm{DIC} = \partial_z \overline{\mathrm{DIC}} + \partial_z \mathrm{DIC}', \tag{10}$$

where primes denote detrended monthly anomalies and overbars denote long-term means. We can decompose the time varying vertical transport of DIC, $\gamma_{\mathrm{DIC}}(w_{50}\partial_z \mathrm{DIC})$, into three Reynolds' terms:

$$\gamma_{\mathrm{DIC}}(w_{50}\partial_z \mathrm{DIC})' = \gamma_{\mathrm{DIC}}(\overline{w_{50}}\partial_z \mathrm{DIC}' + w'_{50}\partial_z \overline{\mathrm{DIC}} + w'_{50}\partial_z \mathrm{DIC}') \tag{11}$$

For models, we can compute all three Reynold's terms. However, for observations-based data products, we can only compute the second Reynold's term ($w'_{50}\partial_z \overline{\mathrm{DIC}}$) since gridded DIC data are only available as a climatology. Therefore, only the second Reynolds' terms are compared.

3 Results

A large region of FCO_2 outgassing can be seen in the equatorial Pacific Ocean, with the highest, (positive, red) values being in the eastern region in SeaFlux (Figure 1a). Comparing mean fluxes, three models (MRI-ESM2-0, MPI-ESM-1-2-HAM and UKESM1-0-LL) are shown in Figure 1b. The models have similar patterns to SeaFlux to the first order, with a basin-wide outgassing feature seen over the equatorial Pacific region, and the largest values lying in the eastern region. Similar maps for all the CMIP6 models are available in Figure S1. Model mean fluxes in the equatorial Pacific are typically weaker than SeaFlux, with the exception of UKESM1-0-LL which has a mean magnitude closer to SeaFlux (the CESM2 family of models also have comparable mean FCO_2 values, Figure S1). The mean outgassing in the equatorial region is noticeably weaker in MRI-ESM2-0 than the other models, and the MPI models show a narrow band of near-zero flux at the equator in the middle of the broader equatorial outgassing pattern.

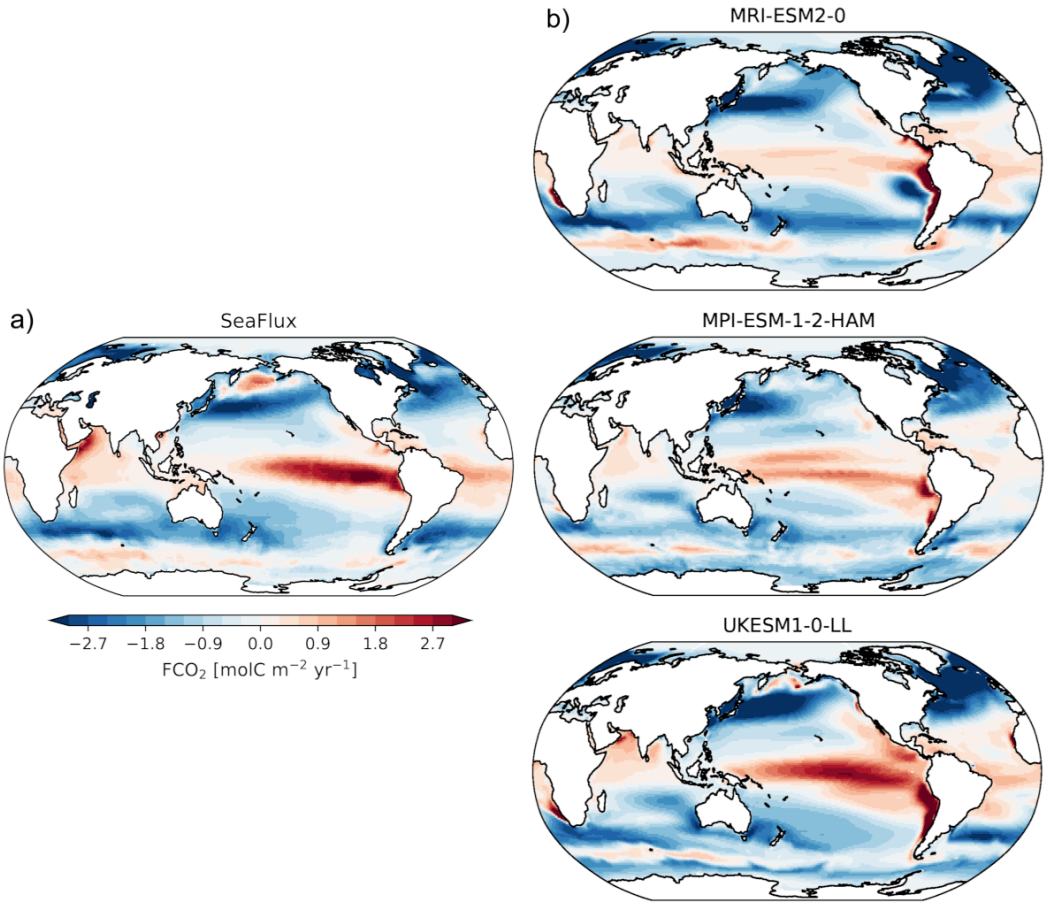

Figure 1. Multiyear mean maps of air-sea CO_2 flux (FCO_2 units: mol C m^{-2} yr^{-1}) taken over 1990-2014 for: a) the SeaFlux ensemble-average, and b) three CMIP6 models (one member was chosen per model): MRI-ESM2-0, MPI-ESM-1-2-HAM and UKESM1-0-LL. Positive values (red) represent fluxes from the ocean to the atmosphere. Similar maps for the remaining CMIP6 models are in Figure S1.

3.1 pCO_2 Interannual Variability and Multiyear Means

The outgassing of CO_2 in the equatorial Pacific Ocean (Figure 1) is modulated by ENSO variability, which dominates the variability of global oceanic FCO_2 (Landschützer et al., 2016; McKinley et al., 2017; McKinley et al., 2004). Amplitudes of FCO_2 IAV ($\sigma_{FCO_2'}$) in the TPI region in CMIP6 differ from SeaFlux observations-based data products (Figure 2a). The majority of CMIP6 models underestimate FCO_2 IAV relative to SeaFlux over the TPI region with the exception of CESM2, CESM2-FV2, CNRM-ESM2-1 and MIROC-ES2L, which have members with FCO_2 IAV amplitudes that overlap with SeaFlux.

FCO_2 is a function of surface ocean and atmospheric pCO_2, and in the parameterization used in the models and data products, has a quadratic relationship to near-surface wind speeds, u_{10} (Wanninkhof, 2014). To investigate the underestimation of FCO_2 seen in CMIP6, we assess their amplitudes of pCO_2 and u_{10} IAV: $\sigma_{pCO_2'}$ and $\sigma_{u_{10}'}$, respectively (see Figure 2b, c). Similar to the FCO_2 IAV estimates, the majority of CMIP6 models underestimate pCO_2 IAV relative to SeaFlux. Meanwhile, u_{10} IAV is overestimated across the majority of models, with the exception of the CanESM5 models, the MPI models, and some smaller underestimation discrepancies from the GFDL-CM4 and MRI-ESM2-0 models, relative to three wind reanalysis data products. The underestimation in modeled pCO_2 IAV appears to be compensated by the overestimation in u_{10} IAV. In the MPI models, pCO_2 IAV is within range of data products, but FCO_2 is low due to low u_{10} IAV.

ENSO-driven variability has a concomitant effect on SST variability in the equatorial Pacific via the upwelling of cool waters. Figure 2d shows that the majority of CMIP6 models overestimate SST IAV in the TPI region, relative to ORAS5 and HadISST estimates. Models that underestimate pCO_2 IAV also overestimate SST IAV, with the exception of the CanESM5 models which underestimate both SST and pCO_2 IAV. Models also tend to overestimate u_{10} variance (Figures 2c, d). This is consistent with the coupling of wind speeds and SST variability via the Bjerknes feedback, where they amplify each other's anomalies.

Multiyear mean maps of pCO_2, averaged over 1990 to 2014, are plotted for SeaFlux and five of the CMIP6 models (Figure 3; Figure S2: all models). A spatial correlation coefficient (SCC) over the TPI region is calculated between each model and SeaFlux to quantify the model skill at reproducing the mean pCO_2 pattern. Note that a high SCC score does not indicate that the magnitude of the mean maps are similar. Generally, the majority of models produce the high pCO_2 equatorial structure seen in SeaFlux, with a third of models having an SCC score above 0.8 (Figure S2). The largest pCO_2 values are seen off coastal Peru and Panama in SeaFlux, with exaggerated coastal values seen in some of the models (ACCESS-ESM1-5, MRI-ESM2-0, and UKESM1-0-LL). Unlike SeaFlux, the high pCO_2 equatorial structure extends almost all the way across the basin in the majority of models, except for the NorESM2 models. Similar to the FCO_2 multiyear mean maps, the MPI models show mean pCO_2 structures that exhibit an equatorial band of low pCO_2 that splits up the general high pCO_2 structure seen in SeaFlux and the other models.

3.2 Spatial Patterns of pCO_2 IAV

The EOF1 of SeaFlux (Figure 4: top left) explains 41% of the total variance in pCO_2 IAV in the tropical Pacific, with a pattern that resembles that of ENSO variability of FCO_2 (McKinley et al., 2004; Resplandy et al., 2015). Its corresponding first principal component (PC1) is highly correlated with ORAS5 SST anomalies in the TPI region ($r = -0.82$, see Figure S3 for PC1 results), which indicates ENSO-driven variability in the tropical Pacific Ocean in the observations-based products.

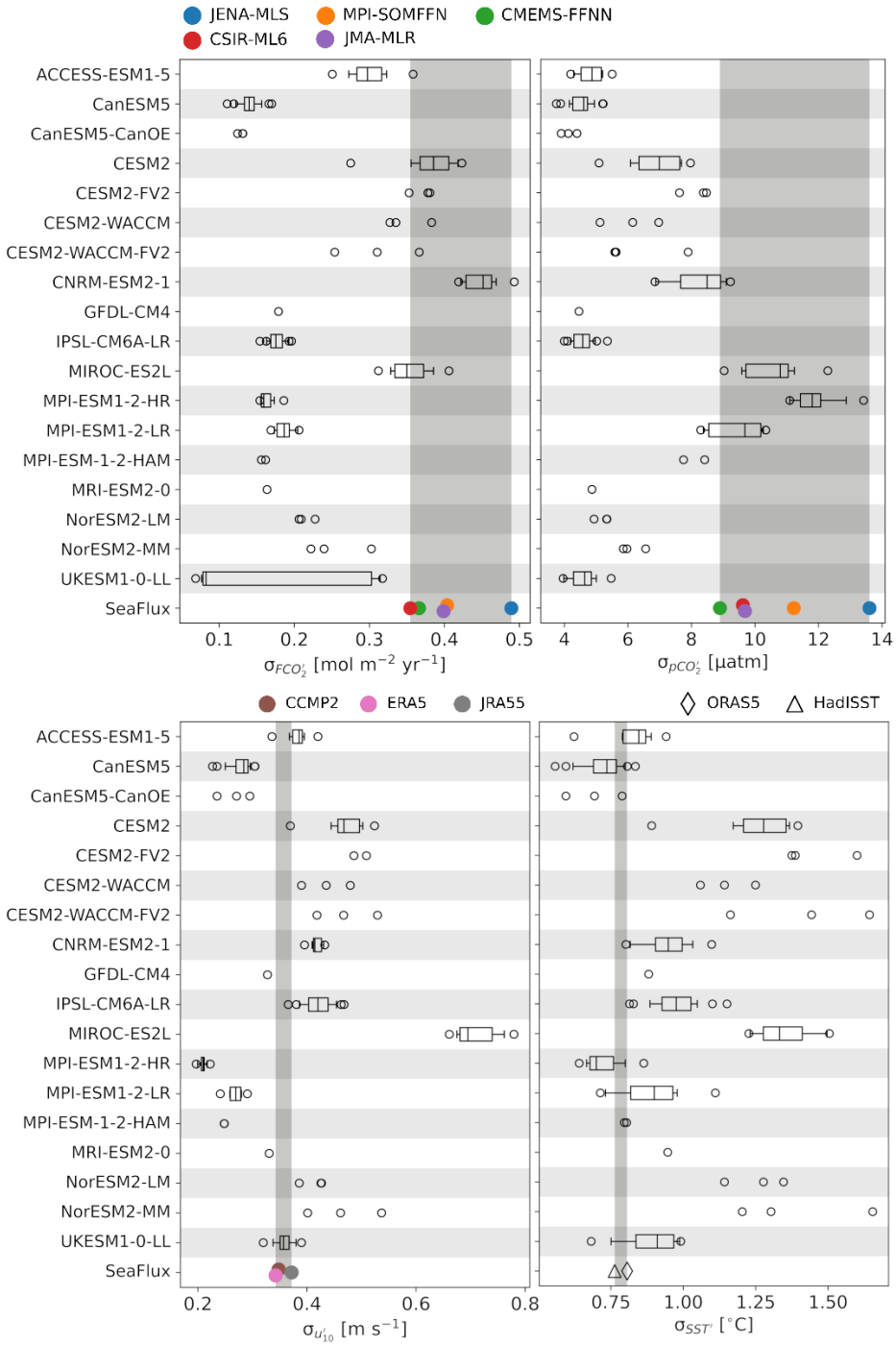

Figure 2. Comparison of IAV amplitudes in models (one standard deviation over the 1959-2014 period), and in observations-based data products (one standard deviation over the 1990-2014 period) in the Tropical Pacific Index (TPI) region (5°N-5°S, 180°E-270°E). Top-left: FCO_2 IAV (units: mol C m^{-2} yr^{-1}); top-right: pCO_2 IAV (units: μatm); bottom-left: u_{10} IAV (units: $m\ s^{-1}$); bottom-right: SST IAV (units: °C). Boxplots represent the spread in IAV amplitudes within a model's ensemble members. For models where fewer than three members were available, the spread is shown without a boxplot. observations-based data products are represented as the filled circles and the grey shaded regions indicate the range of IAV amplitudes within the observations-based data products.

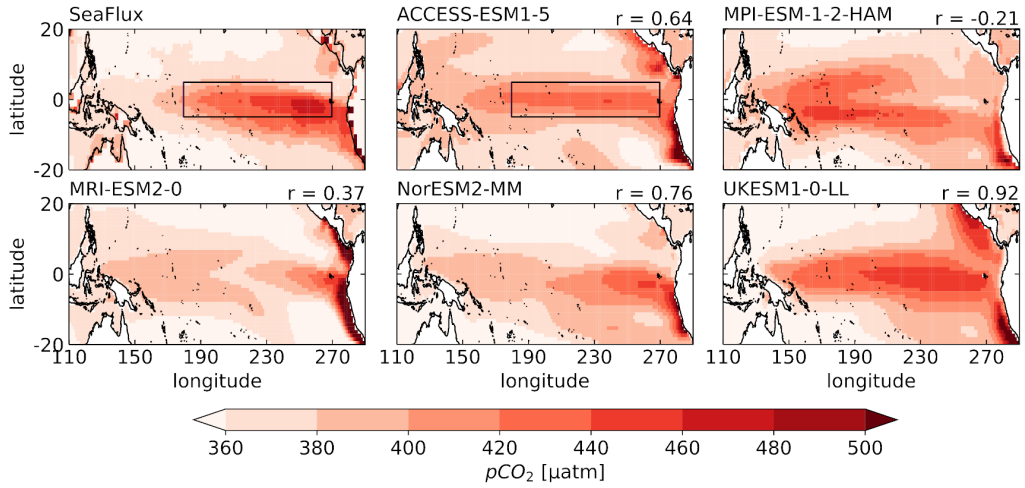

Figure 3. Tropical Pacific pCO_2 multi-year means from 1990-2014 (units: μatm) from the SeaFlux ensemble average (top left) and five CMIP6 models (other panels). Boxes in the SeaFlux and ACCESS-ESM1-5 panels mark the TPI region. The number (r) on the top right of each model's map is the SCC between the model and SeaFlux in the TPI region. Model multi-year means are evaluated using a single ensemble member per model. Similar maps for all CMIP6 models are in Figure S2.

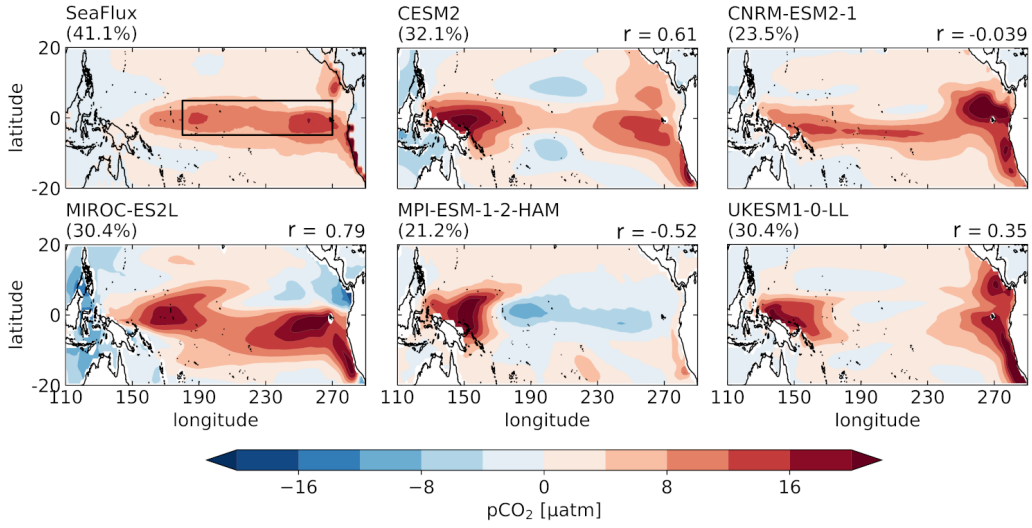

Figure 4. The first EOFs (units: μatm) of detrended pCO_2 anomalies in SeaFlux, averaged across the ensemble (top left), and 5 CMIP6 models (other panels). Model EOF patterns are calculated individually for each ensemble member before averaging over the ensemble. The percentage of the total variance in the tropical Pacific explained by EOF1 is given in parentheses above each panel. The number (r) on the top right of each model's panel is the SCC over the TPI region between each model's EOF1 and SeaFlux's EOF1. The TPI region is shown by the box in the top-left panel. Similar maps for all CMIP6 models are in Figure S4. The corresponding PC1 timeseries are shown in Figure S3.

In CMIP6, few models have an EOF1 that resembles the ENSO pattern seen in SeaFlux (Figure 4; Figure S4: all models). Further, models that have a realistic spatial pattern have too little variance in the first EOF mode. For example, MIROC-ES2L has an EOF1 pattern most similar to SeaFlux (SCC = 0.79), and explains 30% of the total pCO_2 variance. The CESM2 models, CNRM-ESM2-1 and UKESM1-0-LL reveal almost two-centers of action – near the coastlines on either side of the tropical Pacific - for pCO_2 variance. The weak correlation over the TPI region between SeaFlux and CNRM-ESM2-1 (SCC $= -0.04$) is because the positive pCO_2 variance in the model's EOF1 is shifted slightly south of the equator. MPI models show a "negative" EOF1 pattern, revealing pCO_2 variability that is opposite to what is expected from ENSO variability - i.e. the pCO_2 and SST variability in its TPI region are positively correlated, in contrast to the negative correlation in SeaFlux.

Models that reproduce a realistic multiyear mean pCO_2 map (Figure 3), with respect to SeaFlux, do not necessarily have a realistic ENSO pattern of variability (Figure 4). Nevertheless, the relationship between PC1 and TPI SST anomalies do tend to be strong, with a median correlation of r $= -0.73$ (Figure S3). This is consistent with the ENSO signal where upwelling dominates pCO_2 variability (Feely et al., 2006; Sutton et al., 2014).

Figure 5 compares maps of the local correlation coefficient between pCO_2 and SST anomalies in models for the tropical Pacific. These correlations reveal the relative magnitude of $pCO_{2,T}$ and $pCO_{2,nonT}$ components of pCO_2 variability, since the dominance of either component will result in a correlation coefficient that is either positive (thermally dominant) or negative (non-thermally dominant). The strong, negative correlation pattern (blue areas) over the equatorial Pacific, seen in SeaFlux (Figure 5: top left), indicates variability in upwelling of water that is both cool and DIC-rich with ENSO oscillations. Areas of positive correlations (red areas) indicate pCO_2 variability that is thermally driven; warmer SSTs drive higher pCO_2 levels. The negative pCO_2-SST relationship covers a broad region in SeaFlux that spans the basin, with the strongest negative correlations at the equator. Compared to SeaFlux, MIROC-ES2L shows a pattern that covers a similar longitudinal span, however, the intensity of the negative correlations are not as strong, and does not extend as far north. NorESM2-MM shows stronger correlations; however, its negative pattern does not cover the same longitudinal span as seen in SeaFlux. The lack of the negative pCO_2-to-SST extension to the west, common to most of the CMIP6 models, indicates that the ENSO-CO_2 co-variability lies more east in models than in SeaFlux. CNRM-ESM2-1, UKESM1-0-LL and ACCESS-ESM1-5 have a positive correlation zone within the Niño 3.4 region; CESM2 also has an anomalous positive correlation zone that lies more towards the east (Figure S5).

3.3 Thermal and Non-thermal pCO_2 IAV

For SeaFlux and the CMIP6 models, detrended pCO_2 monthly anomalies decomposed into thermally ($pCO_{2,T}$) and non-thermally ($pCO_{2,nonT}$) driven anomalies (Equation 1, 2) indicate the relative magnitudes of thermally and non-thermally driven pCO_2 variability (Figure 6: IPSL-CM6A-LR; S6: other models).

In SeaFlux, $pCO_{2,T}$ ($pCO_{2,nonT}$) anomalies are strongly, positively (negatively) correlated with SST anomalies, with correlation coefficients greater than 0.98. The total pCO_2 anomaly (Figure 6, bold black line) is strongly negatively correlated (r $= -0.92$) with TPI SST anomalies, due to the non-thermal component being dominant over the thermal component ($\sigma_{\mathrm{pCO'_{2,nonT}}} > \sigma_{\mathrm{pCO'_{2,T}}}$).

In contrast, in IPSL-CM6A-LR (Figure 6: right), the non-thermal and thermal components have similar amplitudes but opposite sign ($\sigma_{\mathrm{pCO'_{2,nonT}}} \sim \sigma_{\mathrm{pCO'_{2,T}}}$). This results in the total pCO_2 anomaly having almost no correlation (r $= -0.03$) with SST anomalies. $pCO_{2,T}$ variability almost completely counteracts $pCO_{2,nonT}$ variability, resulting

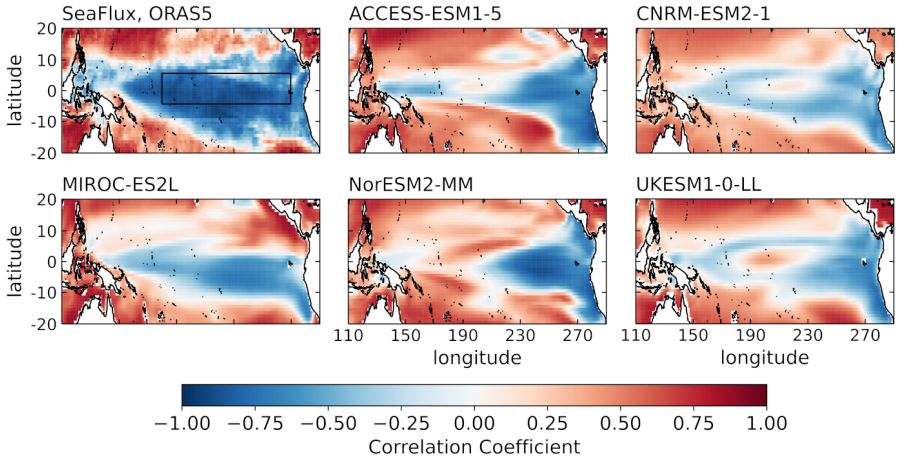

Figure 5. Correlation maps of detrended, pCO_2 and SST monthly anomalies over the tropical Pacific region. Time periods used: 1990-2014 for SeaFlux and ORAS5 (top-left), and 1959-2014 for models (other panels). Model correlation maps were calculated individually for each ensemble member before averaging over the ensemble. For the observations-based map, the mean across SeaFlux pCO_2 products was first taken before correlating with ORAS5 SSTs. Maps for all models are in Figure S5

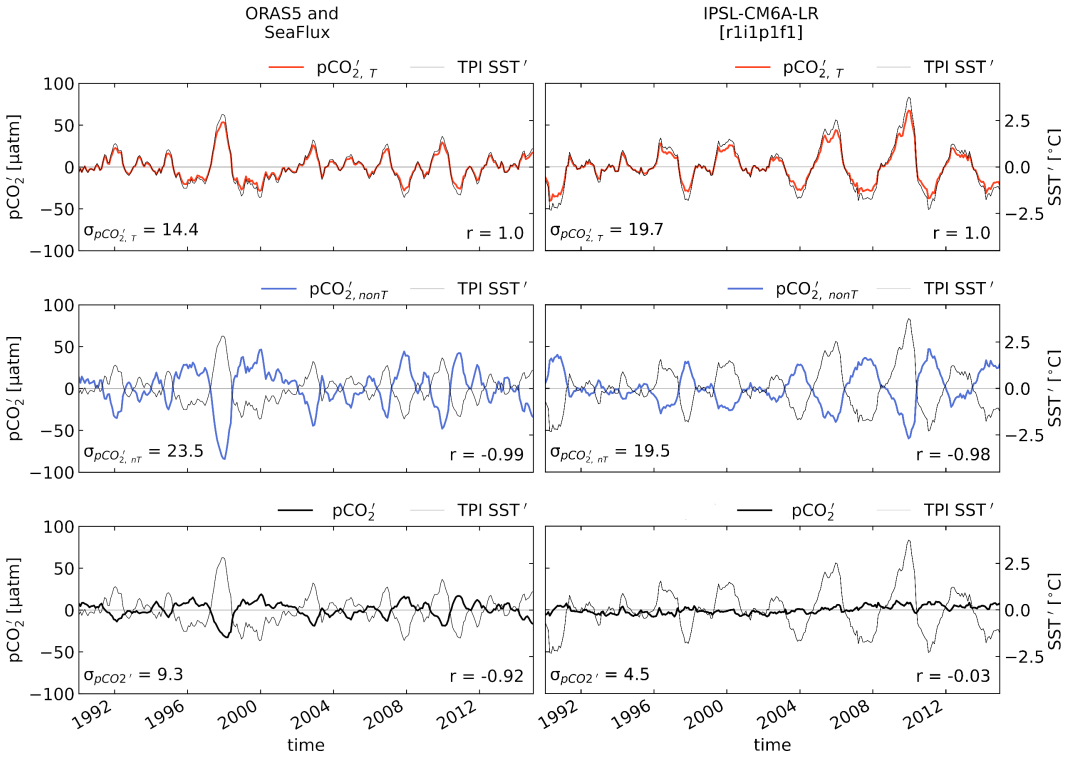

Figure 6. Timeseries of thermal, non-thermal and total pCO_2 anomalies from an ensemble average of the SeaFlux products (left) and from a single member of IPSL-CM6A-LR (right); (top, red) $pCO_{2,T}$ anomalies; (middle, blue) $pCO_{2,nonT}$ anomalies; (bottom, black) net pCO_2 anomalies (units: μatm). All panels are overlaid with the TPI region's SST anomalies (units: °C; the SST y-axis is located on the right side of each panel). The bottom-left number in each panel is the IAV amplitude (σ) of each timeseries, and the bottom-right number is the correlation coefficient (r) of the pCO_2 anomalies with the SST anomalies.

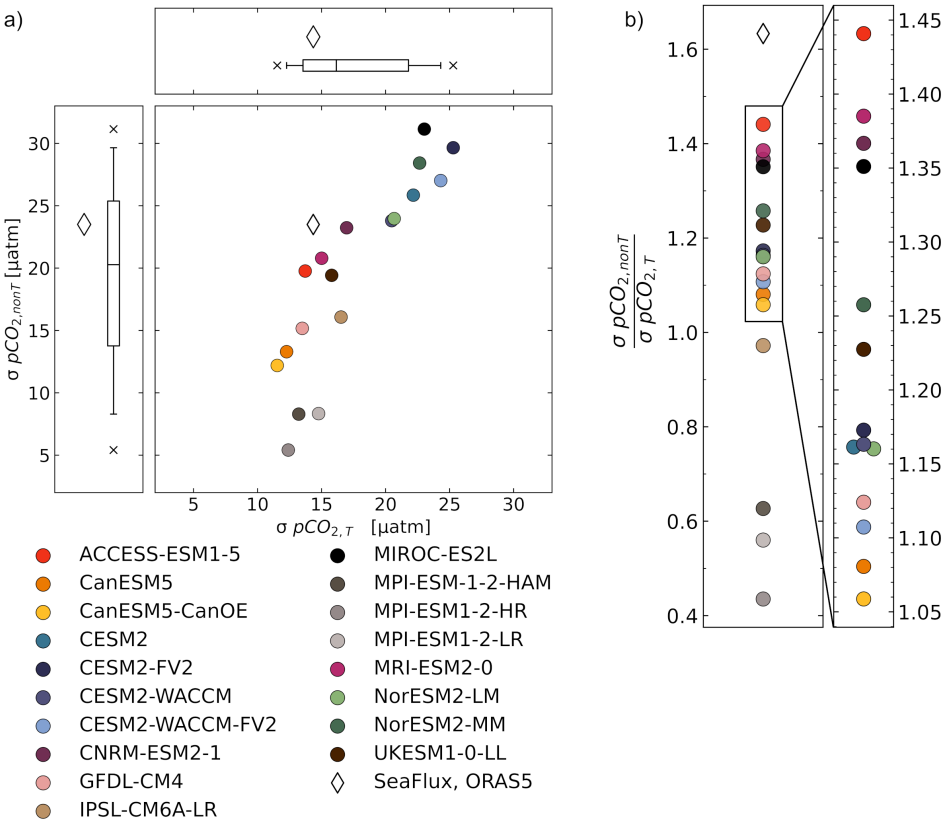

Figure 7. a) Amplitudes of $pCO_{2,T}$ IAV (x-axis) versus $pCO_{2,nonT}$ IAV (y-axis) averaged over the TPI region (units: μatm). Model ensemble means are represented by the filled circles, while the unfilled diamond represents the observations-based data products. Box plots around the figure show the distribution among models for $pCO_{2,T}$ and $pCO_{2,nonT}$ IAV amplitudes. b) Ratios of $pCO_{2,nonT}$ to $pCO_{2,T}$ IAV amplitudes in models (circles) and in the observations-based data products (diamond). Each scatter point represents the ensemble average for models and SeaFlux. The overlaid rectangle is magnified to see the models better.

in a weak total pCO_2 anomaly in IPSL-CM6A-LR. pCO_2 components in other CMIP6 models are also plotted (Figure S6). A summary plot of the relative amplitudes of the thermal and non-thermal components is shown in Figure 7.

Figure 7a compares the amplitudes of $pCO_{2,T}$ and $pCO_{2,nonT}$ anomalies across CMIP6 models' ensemble means. $\sigma pCO_{2,T}$ is 14.4 μatm for SeaFlux-ORAS5, and modeled values range from 11.5 to 25.3 μatm, with the multi-model median variance slightly higher than SeaFlux-ORAS5. On the other hand, $\sigma pCO_{2,nonT}$ for SeaFlux-ORAS5 is 23.5 μatm, while modeled $\sigma pCO_{2,nonT}$ ranges from 5.40 to 31.1μatm with a multi-model median variance lower than that of SeaFlux-ORAS5. Figure 7b compares the ratios of $\sigma pCO_{2,nonT} : \sigma pCO_{2,T}$ in models against the ratio found in the observations-based data products; SeaFlux-ORAS5 has a ratio of 1.63, while the models all have smaller ratios, ranging from 1.44 (ACCESS-ESM1-5) to 0.44 (MPI-ESM1-2-HR). As such, compared to SeaFlux, modeled $\sigma pCO_{2,nonT}$ variability are not appropriately balanced against $\sigma pCO_{2,T}$. Models with a more dominant non-thermal component, i.e. $\sigma pCO_{2,nonT} : \sigma pCO_{2,T}$ ratios closer to SeaFlux-ORAS5, have total pCO_2 anomalies that are more negatively correlated with TPI SST anomalies (Figure S6).

3.4 pCO_2 Correlations with Other Variables

We evaluate the co-variability of ENSO-related variables with pCO_2 in order to better understand the controls on $pCO_{2,T}$ and $pCO_{2,nonT}$ in models versus observations-based data products. Reduced upwelling brings less cool, DIC-rich water to the surface, resulting in warmer SSTs and reduced surface ocean pCO_2. The winds that drive upwelling also force thermocline anomalies; thus, z_{therm} anomalies are positive (deeper) in the TPI region when the trades relax and upwelling weakens.

Correlations of SST, z_{therm}, and w_{50} anomalies with pCO_2 anomalies in the TPI region for SeaFlux are consistent with ENSO-driven variability as described above (Figure 8a), indicating that the observations-based products have realistic relationships between these variables and pCO_2, in particular with SST. For CMIP6, there is a large spread in correlations with pCO_2. NorESM2-MM and MIROC-ES2L have correlations similar to those seen in the observations-based data products. Models with incorrect correlation signs imply a lack of realistic relationships between these physical variables and pCO_2. For example, IPSL-CM6A-LR, and the MPI models have incorrect correlation signs between pCO_2 and the variables considered here. Models with the weakest $pCO_{2,nonT}$ variances (Figure 7a) tend to be the same models with weak or wrong-sign correlations, or did poorly in other areas throughout this assessment (Figures 3-5). On the other hand, models with the strongest $pCO_{2,nonT}$ variances had non-thermal:thermal ratios closest to SeaFlux-ORAS5 (Figure 7). We leave out models that have incorrect correlation signs (negative) for pCO_2 and w_{50} anomalies (Figure 8) when looking at the vertical transport of DIC, since these models do not have realistic pCO_2-upwelling relationships.

3.5 Vertical Ocean Transport of DIC

Despite having higher $pCO_{2,nonT}$ variances in the better performing models, the balances between the non-thermal and thermal components of pCO_2 variability are still not the same as seen in SeaFlux-ORAS5 (Figure 7b). The balance between these components are such that for a given magnitude of $pCO_{2,T}$ IAV, the relative magnitude of $pCO_{2,nonT}$ IAV in models are insufficient to produce the total pCO_2 IAV seen in SeaFlux. This motivates the rest of this assessment where we take a closer look at the vertical transport of DIC and its contribution to $pCO_{2,nonT}$ variability.

In Figure 9a, timeseries for each term in the Reynolds' decomposition (Equation 11) of the vertical transport of DIC in a single model (CESM2) are plotted against the time-tendency of $pCO_{2,nonT}$. Figure 9b shows what can be obtained from data, which is just the second Reynolds term involving the climatological vertical DIC gradient and variable upwelling (Equation 11, second term on right). With Reynolds' decomposition, we are able to isolate in models the contributions from variability in the vertical DIC gradient (Figure 9a: first panel) and the contributions from upwelling variability (Figure 9a: second panel) to the time-tendency of $pCO_{2,nonT}$, $\partial_t pCO'_{2,\mathrm{nonT}}$. The non-linear term (Figure 9a: third panel) is small. The fourth panel in Figure 9a compares the total anomaly of the vertical ocean transport of DIC against $\partial_t pCO'_{2,\mathrm{nonT}}$. In CESM2, the first two Reynolds terms are roughly the same in magnitude, with standard deviations 2.65 and 2.77 times larger than the standard deviation of $\partial_t pCO_{2,\mathrm{nonT}}$. The non-linear term is approximately the same magnitude as $\partial_t pCO_{2,\mathrm{nonT}}$. The total anomaly (Figure 9a: fourth panel) has a standard deviation five times larger than the standard deviation of $\partial_t pCO'_{2,\mathrm{nonT}}$, and has a positive correlation of $r = 0.70$. The magnitude of the total anomaly in vertical DIC transport means that it is important to $pCO_{2,nonT}$ variability, and also that there must be strong damping terms. A summary of the Reynolds' terms in other models is in Table S2. Other models have similar results as CESM2 in that the total anomaly of vertical transport of DIC is significant in magnitude relative to the magnitude of $pCO_{2,nonT}$ variability. Values of their relative magnitudes, σ_{ratio}, range from 2.94 to 5.55 (Table S2),

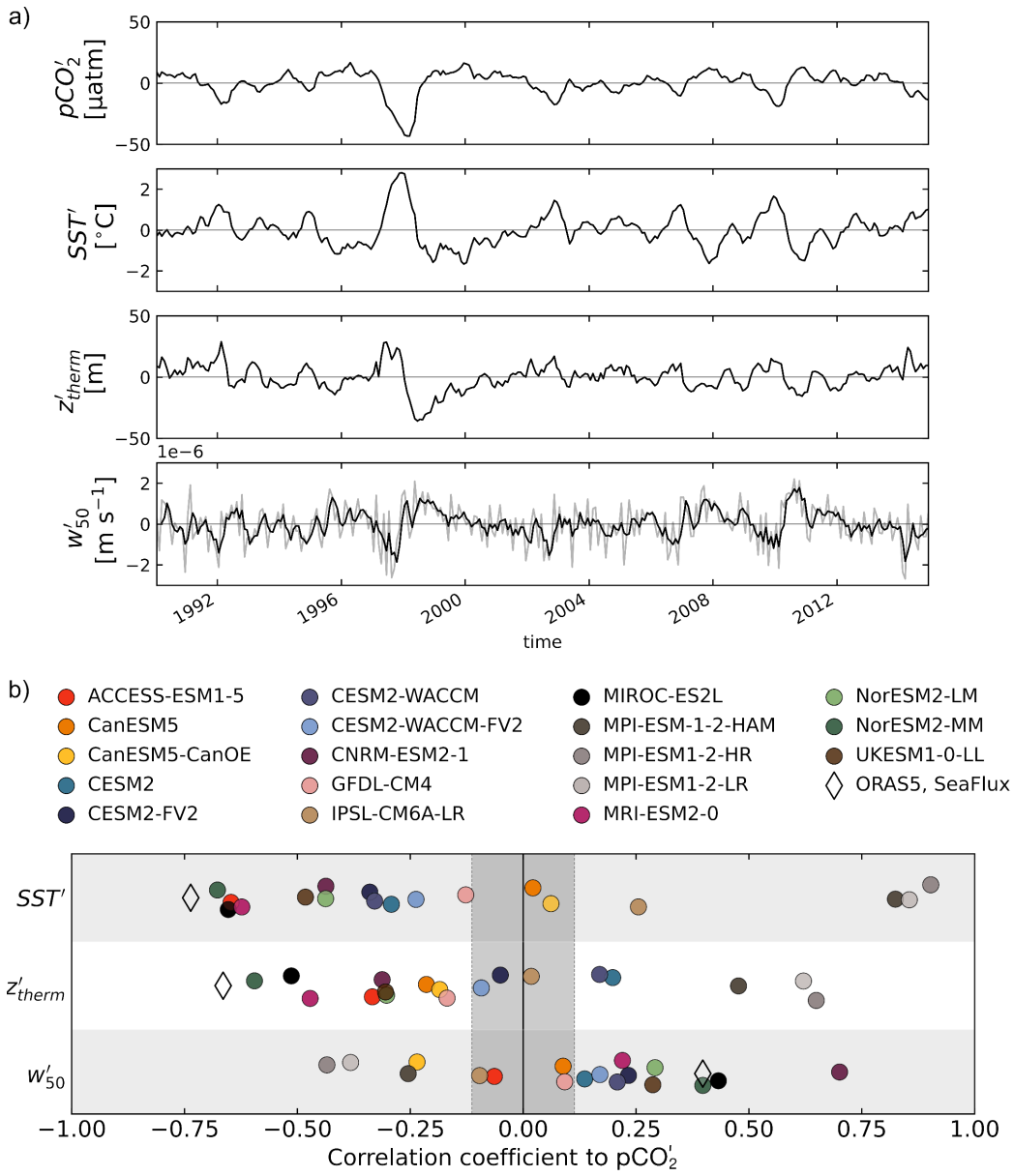

Figure 8. a) Observed timeseries of pCO_2 (units: μatm), SST (units: °C), z_{therm} (units: m), and w_{50} anomalies (units: ms^{-1}) from SeaFlux and ORAS5. A 3-month running mean of w_{50} anomalies is also shown (fourth panel). b) Correlations of pCO_2 to SST, z_{therm}, and w_{50} monthly anomalies over the TPI region. Correlation coefficients for the observations-based data products are marked by the clear diamonds, and the 18 CMIP6 models are marked by filled circles. The model correlation coefficients shown are ensemble means. The grey shading indicates the 95% confidence threshold for the correlations.

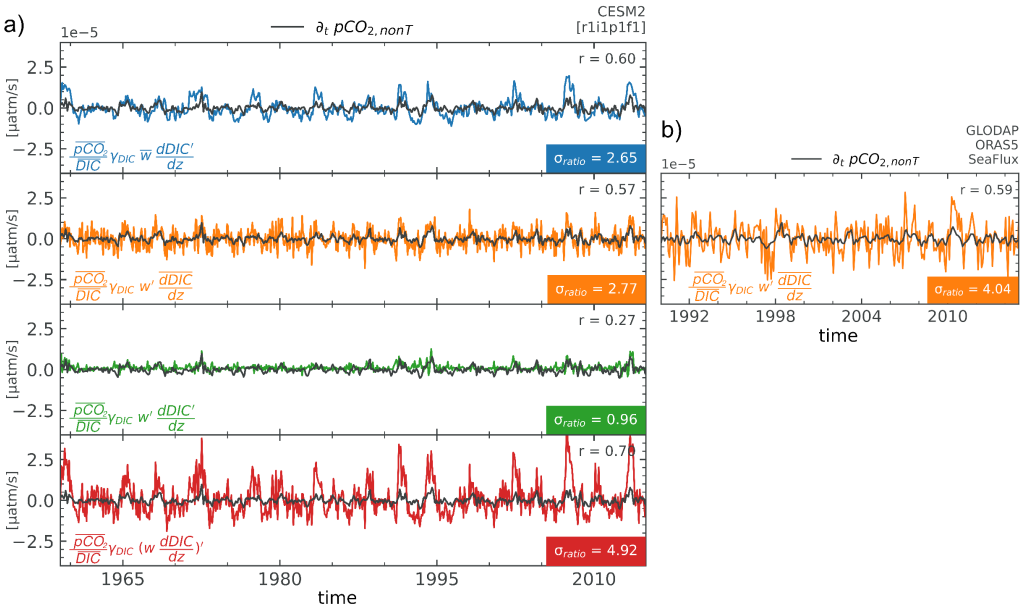

Figure 9. a) Timeseries of the first (blue), second (orange) and third (green) Reynolds' terms from Equation 11, and the full variability is shown in the bottom panel (red) for one member from CESM2 (units: μatm s^{-1}). The time-tendency of $\mathrm{pCO}_{2,nonT}$ is shown in every panel (black line). σ_{ratio} = σ(Reynolds' term)/ $\sigma\partial_t pCO_{2,nonT}'$ is annotated in every panel. The correlation coefficient (r) between the timeseries are also shown. For the other models, a summary of this information can be found in Table S2. b) timeseries of the second Reynolds' term computed from observations-based data products.

which together with strong correlations, means that variability in the vertical transport of DIC is an important source of $\mathrm{pCO}_{2,nonT}$ variability.

Across the models, the first two Reynolds' terms, $\overline{\mathrm{w}_{50}}\partial_\mathrm{z}\mathrm{DIC}'$ and $\mathrm{w}_{50}'\partial_\mathrm{z}\overline{\mathrm{DIC}}$, are the largest terms (Table S2), which suggests that the variability in both upwelling and vertical DIC gradients are similarly important to $\mathrm{pCO}_{2,nonT}$ variability. In MIROC-ES2L, the non-linear term is almost the same amplitude as the first two terms. For observations-based data products, the second Reynolds term ($\mathrm{w}_{50}'\partial_\mathrm{z}\overline{\mathrm{DIC}}$) has a standard deviation four times bigger than the standard deviation of the observations-based $\partial_\mathrm{t}\mathrm{pCO}_{2,\mathrm{nonT}}'$ (Figure 9b). Compared to the observations-based data products, the $\mathrm{w}_{50}'\partial_\mathrm{z}\overline{\mathrm{DIC}}$ term is weak in models (Table S2, second column), except for UKESM1-0-LL. This could be due to either a weak vertical gradient of climatological DIC, or weak upwelling variability, or a combination of both.

A time-averaged vertical velocity section from ORAS5 (Figure S7a) reveals that the depth at which upwelling occurs is within the upper 100m, with a maxima between 50 to 75m at 220°E. We compare upwelling variability in models versus ORAS5 in Figure 10a at 50m. We find that the range of upwelling variability across models is comparable and inclusive of the upwelling variability seen in ORAS5. In contrast, Figure 10b compares the vertical gradient of climatological DIC at 50 m to GLODAPv2. All the models have weaker gradients. We repeat this comparison at 80 m (Figure S8) and confirm that it is robust. Modeled vertical gradients of climatological DIC are biased weak, causing the second Reynolds term ($\mathrm{w}_{50}'\partial_\mathrm{z}\overline{\mathrm{DIC}}$) in models to be weaker than the observations-based estimate (Figure 9; Table S2). To summarize, the second Reynold's term ($\mathrm{w}_{50}'\partial_\mathrm{z}\overline{\mathrm{DIC}}$) is an important term in the overall variability of the vertical transport of DIC, which is

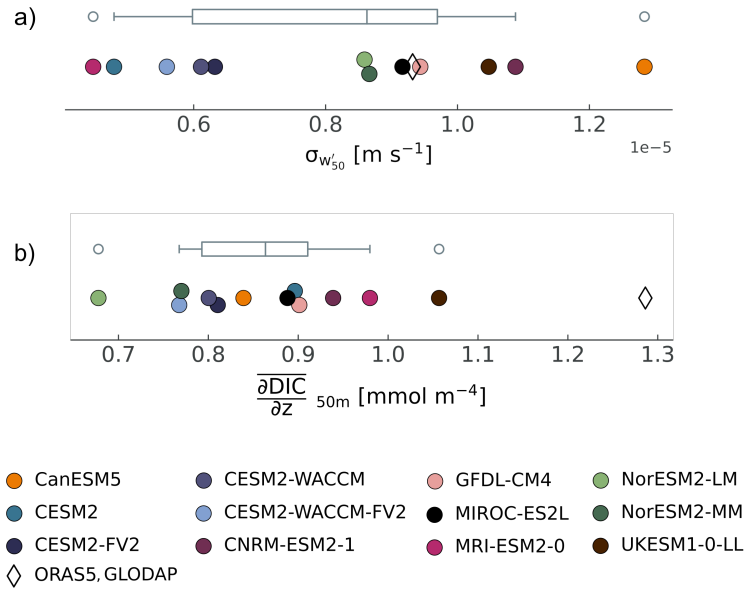

Figure 10. a) Amplitudes (units: ms^{-1}) of upwelling IAV across models (filled circles are one member per model) versus ORAS5 (diamond). b) Amplitudes (units: mmolm^{-4}) of vertical gradients of climatological DIC across models versus GLODAPv2. The boxplots represent the CMIP6 models.

important to the variability in $pCO_{2,nonT}$, and thus pCO_2 variability. Underestimations in $w'_{50}\partial_z\overline{DIC}$ may result in an underestimation in pCO_2 variability.

Alongside modeled mean vertical DIC gradients, we plot the mean vertical temperature gradients ($\partial_z\overline{T}$) at 50m depth to compare the relative strengths of gradients in models, and to identify model biases from observations-based data products (Figure 11a). Vertical temperature gradients are negative since ocean temperatures decrease with depth. The spread in strengths of modeled temperature gradients encompasses that seen in ORAS5, though the majority of models have weaker temperature gradients. The percentage difference between ORAS5 and the models' median temperature gradient is about 21%. For the vertical gradient of climatological DIC, all models underestimate it compared to GLODAPv2, and the ensemble median has a percentage difference of about 39%. While the models tend to underestimate both the vertical gradients of climatological DIC and temperature, the climatological DIC gradients are more weakly biased, which for a given upwelling will tend to result in weaker $pCO_{2,nonT}$ variability relative to $pCO_{2,T}$.

Figure 11b compares the influence of $w'_{50}\partial_z\overline{T}$ against the influence of $w'_{50}\partial_z\overline{DIC}$ on pCO_2 using the coefficients from Equation 7. Contributions from $w'_{50}\partial_z\overline{DIC}$ to pCO_2 in models are about 6 times greater than the thermal contributions. The vertical DIC term is much bigger than the vertical T term, but the asscoiated $pCO_{2,nonT}$ variability is not proportionally bigger than $pCO_{2,T}$ variability. Thus, weak vertical gradients cannot fully explain the $pCO_{2,nonT}$, $pCO_{2,T}$ differences. Daily pCO_2 variability (σpCO_2) in the TPI region in SeaFlux is 0.35 μatm day^{-1}, and values in models range from 0.29 to 0.46 μatm day^{-1} (not shown). These values of daily TPI pCO_2 variability are on the same order of magnitude as the $w'_{50}\partial_z\overline{DIC}$ contributions to pCO_2 (Figure 11b: y-axis). In observations, and in some models, $w'_{50}\partial_z\overline{DIC}$ contributions to pCO_2 are greater than the daily pCO_2 variability in the TPI region. In observations, and in some models, $w'_{50}\partial_z\overline{DIC}$ contributions to pCO_2 are larger than daily pCO_2 variability in the TPI region. This

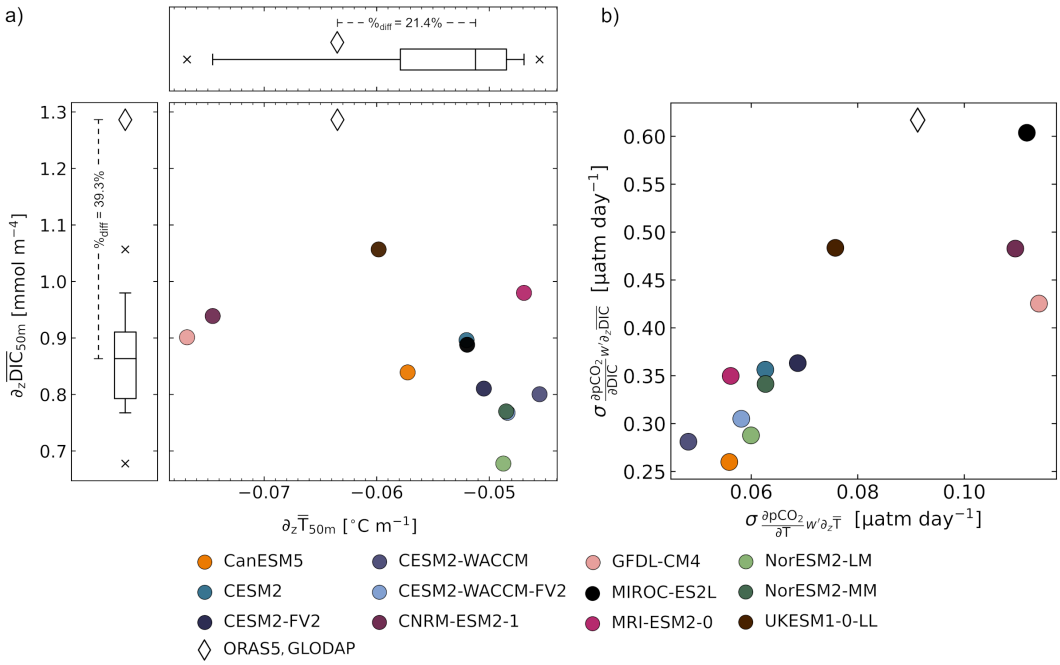

Figure 11. a) The relative strength of vertical mean temperature gradients (x-axis, units: $^{\circ}\mathrm{Cm}^{-1}$) against vertical climatological DIC gradients (y-axis, units: mmolm^{-4}) in 12 CMIP6 models (filled circles represent a single ensemble member) and in ORAS5 versus GLODAPv2 data (clear diamond). The boxplots represent the distribution in gradients among models, excluding observations-based data products (clear diamonds). b) The vertical transport of the climatological vertical temperature gradient versus the DIC gradient, converted into units of μatm day^{-1}.

means that significant damping of pCO_2 must be happening in order for it to be underestimated, despite the large contribution from the vertical transport of DIC.

4 Discussion

The majority (15) of the 18 CMIP6 models underestimate pCO_2 IAV, while they overestimate SST IAV. FCO_2 IAV is also underestimated by the majority of CMIP6 models. Previous studies of historical simulations from the earlier CMIP5 found that FCO_2 IAV were also underestimated in models (Dong et al., 2016, 2017). Results from another CMIP6 study also find that most models simulate weak FCO_2 anomalies while overestimating SST IAV (Vaittinada Ayar et al., 2022).

We find that the correlations between pCO_2 and other ENSO-related variables vary. Most models have correlations weaker than observed over the TPI region, a few are consistent with observations, and another few are opposite to observed. Weak ENSO-driven relationships were also noted in previous CMIP5 studies (Dong et al., 2017; Jin et al., 2019). Dong et al. (2016) also found that 12 models out of the 18 CMIP5 subset failed to show ENSO characteristics in FCO_2 variability. They also found that models differed among themselves the most in regions with strong vertical movement, such as the tropical Pacific.

Modeled $pCO_{2,nonT}$ variance in CMIP6 is not appropriately balanced with $pCO_{2,T}$ variability. Weak $pCO_{2,nonT}$ anomalies are insufficient to counteract the $pCO_{2,T}$ anoma-

lies resulting in total pCO_2 anomalies that are too weak. In the equatorial Pacific, Jin et al. (2019) found pCO_2 biases in two CMIP5 models that resulted from weak DIC contributions to pCO_2. Weak DIC contributions were found to be mainly caused by weak vertical gradients of climatological DIC and weak upwelling anomalies, which both limit the vertical transport of DIC (Jin et al., 2019). We find that upwelling anomalies in CMIP6 are comparable to ORAS5 (Figure 10a).

Changes in the vertical transport of DIC affects surface DIC variability, which is known to be the dominant driver of pCO_2 variability in the surface equatorial Pacific Ocean (McKinley et al., 2004; Liao et al., 2020). We find model pCO_2 anomalies due to variability in the vertical transport of DIC are larger than their $pCO_{2,nonT}$ anomalies by a factor of 3 to almost 6 times (see Table S2: last column) but are positively correlated. This suggests that variability in the vertical transport of DIC is an important source of $pCO_{2,nonT}$ variability in models. At the same time, $w'_{50}\partial_z\overline{DIC}$ contributions to pCO_2 are comparable in magnitude to daily pCO_2 variability in the TPI region (Figure S9b). Together, these findings indicate that $w'_{50}\partial_z\overline{DIC}$ contributions to pCO_2 variability are significantly damped by other processes.

The vertical gradient of climatological DIC is consistently weak across all the models relative to observations-based data products (Figure 10), which is consistent with prior model results from CMIP5 (Jin et al., 2019). Vertical gradients of climatological temperature are not as weak. The imbalance in the relative strengths of these vertical gradients, for a given upwelling anomaly, contributes towards weaker non-thermal pCO_2 variability, relative to the thermal.

While the relative strengths of mean vertical gradients, through upwelling, can result in weaker $\sigma pCO_{2,nonT}$:$\sigma pCO_{2,T}$ ratios, we do not find a linear scaling between the relative strengths in mean vertical gradients and the ratios of $\sigma pCO_{2,nonT}$: $\sigma pCO_{2,T}$ across the models (Figure S9). A linear scaling would indicate that biases in the relative strengths of the mean vertical gradients proportionally bias the pCO_2 ratios. Thus, we find the relative strengths of mean vertical gradients alone do not determine the imbalance in pCO_2 ratios. A more complete assessment that includes the other processes that contribute to pCO_2 variability will be necessary to understand the causes of insufficient $pCO_{2,nonT}$ variability.

Other processes that contribute to equatorial Pacific DIC variability that can dampen $pCO_{2,nonT}$ variability, include the horizontal transport of DIC, biological processes, freshwater fluxes and air-sea CO_2 fluxes. For example, when DIC is bought to the surface via upwelling, though pCO_2 increases, the instantaneous air-sea CO_2 flux response dampens surface DIC concentrations (Liao et al., 2020). The biological response also damps surface DIC concentrations; upwelling of nutrient-rich waters enhances biologically-driven uptake of DIC (Chavez et al., 1999). Freshwater fluxes (rainfall) also dilute surface DIC concentrations, and westward horizontal transport along the equator removes DIC from the upwelling region (Doney et al., 2009).

Aside from DIC, other ocean biogeochemical variables influence surface $pCO_{2,nonT}$, such as alkalinity. Vaittinada Ayar et al. (2022) find that models with strong alkalinity biases have weak surface DIC biases (i.e. weak surface DIC variability), which leads to a reduction in $pCO_{2,nonT}$ variability. They find that for some models (CanESM5, GFDL-CM4 and MRI-ESM2-0), $pCO_{2,nonT}$ variability is weak enough that pCO_T variability can dominate total pCO_2 anomalies. However, an alkalinity bias alone does not explain all the models that underestimate $pCO_{2,nonT}$, relative to $pCO_{2,T}$, as we analyze here. For example, Vaittinada Ayar et al. (2022) shows that IPSL-CM6A-LR doesn't have a strong alkalinity bias, however, we find that its $pCO_{2,nonT}$:$pCO_{2,T}$ variance ratio is weaker than the ratio in MRI-ESM2-0 (Figure 7b), which is a model they show with a strong alkalinity bias.

Vaittinada Ayar et al. (2022) proposed that models without a strong alkalinity bias may be better predictors of future ENSO-CO_2 flux dynamics. However, we find that these models underestimate equatorial Pacific pCO_2 IAV and ENSO-related covariability. For example, IPSL-CM6A-LR did not have realistic correlations between pCO_2 and SST, z_{therm} or w_{50} anomalies (Figure 8b). We propose that a wide range of variables need to be considered when selecting models for analysis of future trends. While this study looks at ENSO-driven pCO_2 IAV, it has relevance for trends. Trends in SSTs, thermocline depths and upwelling in response to rising atmospheric CO_2 involve many of the same coupled dynamics that drive ENSO variability (Seager et al., 2019; Cane et al., 1997; Clement et al., 1996). CMIP6 models cannot reproduce the observed trends in the tropical Pacific physical state and hence it is possible that they are also misrepresenting the trends in pCO_2 and air-sea CO_2 fluxes, with potential influence on the airborne fraction of anthropogenic CO_2. Validating ENSO-driven pCO_2 variability in models is a necessary first step to examining the tropical Pacific's coupled climate-carbon response to anthropogenic climate change.

5 Conclusions

In the equatorial Pacific, weak ENSO-related pCO_2 variability in CMIP6 models is explained by an imbalance between $pCO_{2,nonT}$ and $pCO_{2,T}$ anomalies, whereby $pCO_{2,nonT}$ variability is insufficient to counteract strong $pCO_{2,T}$ variability. Strong $pCO_{2,T}$ variability in CMIP6 is driven by excessive SST variance. Variability in the vertical transport of DIC does matter to $pCO_{2,nonT}$ variability in that upwelling anomalies acting on weak vertical DIC gradients can lead to weaker surface DIC variability. However, this alone does not explain the relative magnitudes of $pCO_{2,nonT}$ and $pCO_{2,T}$ anomalies. To guide model development, assessments of other processes that drive DIC variability will help to identify the causes of significant damping of $pCO_{2,nonT}$ variability that ultimately leads to weak pCO_2 variability in models.

6 Open Research

CMIP6 model output data are available at: http://esgf-node.llnl.gov/projects/cmip6. Information on installing and using the CMIP6 data pre-processing Python package (Busecke & Abernathey, 2020) can be accessed here: https://cmip6-preprocessing.readthedocs.io/en/latest/.

SeaFlux products (including wind speed products) are available on Zenodo: https://doi.org/10.5281/zenodo.5482547. GLODAPv2.2021 data, archived at NOAA-NCEI at https://www.ncei.noaa.gov/access/metadata/landing-page/bin/iso?id=gov.noaa.nodc:0237935, can also be downloaded from the GLODAP website: https://www.glodap.info/. The ECMWF-ORAS5 data set can be downloaded from the Integrated Climate Data Center portal at http://icdc.cen.uni-hamburg.de/thredds/catalog/ftpthredds/EASYInit/oras5/catalog.html and https://www.cen.uni-hamburg.de/icdc/data/ocean/easy-init-ocean/ecmwf-oras5-backward-extension.html for 1979-2018 and 1958-1978, respectively. HadISST data were obtained from https://www.metoffice.gov.uk/hadobs/hadisst/ and are © British Crown Copyright, Met Office (2022), provided under a Non-Commercial Government Licence http://www.nationalarchives.gov.uk/doc/non-commercial-government-licence/version/2/.

Acknowledgments

We acknowledge the World Climate Research Programme, which, through its Working Group on Coupled Modelling, coordinated and promoted CMIP6. We thank the climate modeling groups for producing and making available their model output, the Earth System Grid Federation (ESGF) for archiving the data and providing access, and the multiple funding agencies who support CMIP6 and ESGF. S.W. acknowledges Pangeo for providing cloud-services for this research, and would also like to thank Julius Busecke for their CMIP6 pre-processing Python package. This research was supported in part by the National Science Foundation (OCE 22-19829, OCE-1948624, LEAP STC 2019625). The authors declare that they have no conflict of interest.

References

Bentsen, M., Oliviè, D. J. L., Seland, y., Toniazzo, T., Gjermundsen, A., Graff, L. S., ... Schulz, M. (2019). *NCC NorESM2-MM model output prepared for CMIP6 CMIP historical [Dataset].* Earth System Grid Federation. doi: 10.22033/ESGF/CMIP6.8040

Bjerknes, J. (1966). A possible response of the atmospheric hadley circulation to equatorial anomalies of ocean temperature. *Tellus*, *18*(4), 820-829. Retrieved from https://onlinelibrary.wiley.com/doi/abs/10.1111/j.2153-3490.1966.tb00303.x doi: https://doi.org/10.1111/j.2153-3490.1966.tb00303.x

Boucher, O., Denvil, S., Levavasseur, G., Cozic, A., Caubel, A., Foujols, M.-A., ... Marchand, M. (2021). *IPSL IPSL-CM6A-LR-INCA model output prepared for CMIP6 CMIP historical [Dataset].* Earth System Grid Federation. doi: 10.22033/ESGF/CMIP6.13601

Busecke, J., & Abernathey, R. (2020). Cmip6 without the interpolation: Grid-native analysis with pangeo in the cloud. *Earth and Space Science Open Archive*, 1. Retrieved from https://doi.org/10.1002/essoar.10504242.1 doi: 10.1002/essoar.10504242.1

Byun, Y.-H. (2020). *NIMS-KMA UKESM1.0-LL model output prepared for CMIP6 CMIP historical [Dataset].* Earth System Grid Federation. doi: 10.22033/ESGF/CMIP6.8379

Cane, M. A., Clement, A. C., Kaplan, A., Kushnir, Y., Pozdnyakov, D., Seager, R., ... Murtugudde, R. (1997). Twentieth-century sea surface temperature trends. *Science*, *275*(5302), 957-960. Retrieved from https://www.science.org/doi/

abs/10.1126/science.275.5302.957 doi: 10.1126/science.275.5302.957

Chavez, F. P., Strutton, P. G., Friederich, G. E., Feely, R. A., Feldman, G. C., Foley, D. G., & McPhaden, M. J. (1999). Biological and chemical response of the equatorial pacific ocean to the 1997-98 el niño. *Science*, *286*(5447), 2126-2131. Retrieved from https://www.science.org/doi/abs/10.1126/science.286.5447.2126 doi: 10.1126/science.286.5447.2126

Clement, A. C., Seager, R., Cane, M. A., & Zebiak, S. E. (1996). An ocean dynamical thermostat. *Journal of Climate*, *9*(9), 2190 - 2196. Retrieved from https://journals.ametsoc.org/view/journals/clim/9/9/1520-0442_1996_009_2190_aodt_2_0_co_2.xml doi: 10.1175/1520-0442(1996)009⟨2190:AODT⟩2.0.CO;2

Danabasoglu, G. (2019a). *NCAR CESM2-FV2 model output prepared for CMIP6 CMIP historical [Dataset].* Earth System Grid Federation. doi: 10.22033/ESGF/CMIP6.11297

Danabasoglu, G. (2019b). *NCAR CESM2 model output prepared for CMIP6 CMIP historical [Dataset].* Earth System Grid Federation. doi: 10.22033/ESGF/CMIP6.7627

Danabasoglu, G. (2019c). *NCAR CESM2-WACCM-FV2 model output prepared for CMIP6 CMIP historical [Dataset].* Earth System Grid Federation. doi: 10.22033/ESGF/CMIP6.11298

Danabasoglu, G. (2019d). *NCAR CESM2-WACCM model output prepared for CMIP6 CMIP historical [Dataset].* Earth System Grid Federation. doi: 10.22033/ESGF/CMIP6.10071

Doney, S. C., Lima, I., Feely, R. A., Glover, D. M., Lindsay, K., Mahowald, N., ... Wanninkhof, R. (2009). Mechanisms governing interannual variability in upper-ocean inorganic carbon system and air–sea co2 fluxes: Physical climate and atmospheric dust. *Deep Sea Research Part II: Topical Studies in Oceanography*, *56*(8), 640-655. (Surface Ocean CO2 Variability and Vulnerabilities) doi: https://doi.org/10.1016/j.dsr2.2008.12.006

Dong, F., Li, Y., & Wang, B. (2017). Assessment of responses of tropical pacific air–sea co2 flux to enso in 14 cmip5 models. *Journal of Climate*, *30*(21), 8595 - 8613. Retrieved from https://journals.ametsoc.org/view/journals/clim/30/21/jcli-d-16-0543.1.xml doi: 10.1175/JCLI-D-16-0543.1

Dong, F., Li, Y., Wang, B., Huang, W., Shi, Y., & Dong, W. (2016). Global air–sea co 2 flux in 22 cmip5 models: Multiyear mean and interannual variability. *Journal of Climate*, *29*(7), 2407–2431.

Emori, S., Taylor, K., Hewitson, B., Zermoglio, F., Juckes, M., Lautenschlager, M., & Stockhause, M. (2016). Cmip5 data provided at the ipcc data distribution centre [Computer software manual]. Fact Sheet of the Task Group on Data and Scenario Support for Impact and Climate Analysis (TGICA) of the Intergovernmental Panel on Climate Change (IPCC). Retrieved from http://sedac.ipcc-data.org/ddc/ar5_scenario_process/RCPs.html

Farneti, R., Stiz, A., & Ssebandeke, J. B. (2022, 12). Improvements and persistent biases in the southeast tropical atlantic in cmip models. *npj Climate and Atmospheric Science*, *5*. doi: 10.1038/s41612-022-00264-4

Fay, A. R., Gregor, L., Landschützer, P., McKinley, G. A., Gruber, N., Gehlen, M., ... Zeng, J. (2021). Seaflux: harmonization of air–sea co_2 fluxes from surface pco_2 data products using a standardized approach. *Earth System Science Data*, *13*(10), 4693–4710. Retrieved from https://essd.copernicus.org/articles/13/4693/2021/ doi: 10.5194/essd-13-4693-2021

Feely, R. A., Takahashi, T., Wanninkhof, R., McPhaden, M. J., Cosca, C. E., Sutherland, S. C., & Carr, M.-E. (2006). Decadal variability of the air-sea co2 fluxes in the equatorial pacific ocean. *Journal of Geophysical Research: Oceans*, *111*(C8). Retrieved from https://agupubs.onlinelibrary.wiley.com/doi/abs/10.1029/2005JC003129 doi: https://doi.org/10.1029/

2005JC003129

Friedlingstein, P., Jones, M. W., O'Sullivan, M., Andrew, R. M., Bakker, D. C. E., Hauck, J., ... Zeng, J. (2022). Global carbon budget 2021. *Earth System Science Data*, *14*(4), 1917–2005. Retrieved from https://essd.copernicus.org/articles/14/1917/2022/ doi: 10.5194/essd-14-1917-2022

Guo, H., John, J. G., Blanton, C., McHugh, C., Nikonov, S., Radhakrishnan, A., ... Zhang, R. (2018). *NOAA-GFDL GFDL-CM4 model output historical [Dataset].* Earth System Grid Federation. doi: 10.22033/ESGF/CMIP6.8594

Hajima, T., Abe, M., Arakawa, O., Suzuki, T., Komuro, Y., Ogura, T., ... Tachiiri, K. (2019). *MIROC MIROC-ES2L model output prepared for CMIP6 CMIP historical [Dataset].* Earth System Grid Federation. doi: 10.22033/ESGF/CMIP6.5602

Jin, C., Zhou, T., & Chen, X. (2019). Can cmip5 earth system models reproduce the interannual variability of air–sea co2 fluxes over the tropical pacific ocean? *Journal of Climate*, *32*(8), 2261 - 2275. Retrieved from https://journals.ametsoc.org/view/journals/clim/32/8/jcli-d-18-0131.1.xml doi: 10.1175/JCLI-D-18-0131.1

Jungclaus, J., Bittner, M., Wieners, K.-H., Wachsmann, F., Schupfner, M., Legutke, S., ... Roeckner, E. (2019). *MPI-M MPI-ESM1.2-HR model output prepared for CMIP6 CMIP historical [Dataset].* Earth System Grid Federation. doi: 10.22033/ESGF/CMIP6.6594

Landschützer, P., Gruber, N., & Bakker, D. C. E. (2016). Decadal variations and trends of the global ocean carbon sink. *Global Biogeochemical Cycles*, *30*(10), 1396-1417. Retrieved from https://agupubs.onlinelibrary.wiley.com/doi/abs/10.1002/2015GB005359 doi: https://doi.org/10.1002/2015GB005359

Lauvset, S. K., Lange, N., Tanhua, T., Bittig, H. C., Olsen, A., Kozyr, A., ... Key, R. M. (2021). An updated version of the global interior ocean biogeochemical data product, glodapv2.2021. *Earth System Science Data*, *13*(12), 5565–5589. Retrieved from https://essd.copernicus.org/articles/13/5565/2021/ doi: 10.5194/essd-13-5565-2021

Le Quéré, C., Orr, J. C., Monfray, P., Aumont, O., & Madec, G. (2000). Interannual variability of the oceanic sink of co2 from 1979 through 1997. *Global Biogeochemical Cycles*, *14*(4), 1247–1265.

Li, G., & Xie, S.-P. (2012). Origins of tropical-wide sst biases in cmip multi-model ensembles. *Geophysical Research Letters*, *39*(22). Retrieved from https://agupubs.onlinelibrary.wiley.com/doi/abs/10.1029/2012GL053777 doi: https://doi.org/10.1029/2012GL053777

Liao, E., Resplandy, L., Liu, J., & Bowman, K. W. (2020). Amplification of the ocean carbon sink during el niños: Role of poleward ekman transport and influence on atmospheric co2. *Global Biogeochemical Cycles*, *34*(9), e2020GB006574. Retrieved from https://agupubs.onlinelibrary.wiley.com/doi/abs/10.1029/2020GB006574 doi: https://doi.org/10.1029/2020GB006574

Long, M. C., Lindsay, K., Peacock, S., Moore, J. K., & Doney, S. C. (2013). Twentieth-century oceanic carbon uptake and storage in cesm1(bgc). *Journal of Climate*, *26*(18), 6775 - 6800. Retrieved from https://journals.ametsoc.org/view/journals/clim/26/18/jcli-d-12-00184.1.xml doi: 10.1175/JCLI-D-12-00184.1

Lovenduski, N. S., Gruber, N., Doney, S. C., & Lima, I. D. (2007). Enhanced co2 outgassing in the southern ocean from a positive phase of the southern annular mode. *Global Biogeochemical Cycles*, *21*(2). Retrieved from https://agupubs.onlinelibrary.wiley.com/doi/abs/10.1029/2006GB002900 doi: https://doi.org/10.1029/2006GB002900

McKinley, G. A., Fay, A. R., Lovenduski, N. S., & Pilcher, D. J. (2017). Natural

variability and anthropogenic trends in the ocean carbon sink. *Annual Review of Marine Science*, *9*(1), 125-150. Retrieved from https://doi.org/10.1146/annurev-marine-010816-060529 (PMID: 27620831) doi: 10.1146/annurev-marine-010816-060529

McKinley, G. A., Follows, M. J., & Marshall, J. (2004, June). Mechanisms of air-sea CO_2 flux variability in the equatorial Pacific and the North Atlantic. *Global Biogeochemical Cycles*, *18*(2), GB2011. doi: 10.1029/2003GB002179

Neubauer, D., Ferrachat, S., Siegenthaler-Le Drian, C., Stoll, J., Folini, D. S., Tegen, I., ... Lohmann, U. (2019). *HAMMOZ-Consortium MPI-ESM1.2-HAM model output prepared for CMIP6 CMIP historical [Dataset].* Earth System Grid Federation. doi: 10.22033/ESGF/CMIP6.5016

Rayner, N. A., Parker, D. E., Horton, E. B., Folland, C. K., Alexander, L. V., Rowell, D. P., ... Kaplan, A. (2003). Global analyses of sea surface temperature, sea ice, and night marine air temperature since the late nineteenth century. *Journal of Geophysical Research: Atmospheres*, *108*(D14). Retrieved from https://agupubs.onlinelibrary.wiley.com/doi/abs/10.1029/2002JD002670 doi: https://doi.org/10.1029/2002JD002670

Resplandy, L., Séférian, R., & Bopp, L. (2015). Natural variability of co2 and o2 fluxes: What can we learn from centuries-long climate models simulations? *Journal of Geophysical Research: Oceans*, *120*(1), 384-404. Retrieved from https://agupubs.onlinelibrary.wiley.com/doi/abs/10.1002/2014JC010463 doi: https://doi.org/10.1002/2014JC010463

Rödenbeck, C., Bakker, D. C. E., Metzl, N., Olsen, A., Sabine, C., Cassar, N., ... Heimann, M. (2014). Interannual sea–air co_2 flux variability from an observation-driven ocean mixed-layer scheme. *Biogeosciences*, *11*(17), 4599–4613. Retrieved from https://bg.copernicus.org/articles/11/4599/2014/ doi: 10.5194/bg-11-4599-2014

Sarmiento, J. L., & Gruber, N. (2006). *Ocean biogeochemical dynamics*. Princeton University Press.

Seager, R., Cane, M., Henderson, N., Lee, D. E., Abernathey, R., & Zhang, H. (2019, 7). Strengthening tropical pacific zonal sea surface temperature gradient consistent with rising greenhouse gases. *Nature Climate Change*, *9*, 517-522. doi: 10.1038/s41558-019-0505-x

Seferian, R. (2018). *CNRM-CERFACS CNRM-ESM2-1 model output prepared for CMIP6 CMIP historical [Dataset].* Earth System Grid Federation. doi: 10.22033/ESGF/CMIP6.4068

Séférian, R., Berthet, S., Yool, A., Palmieri, J., Bopp, L., Tagliabue, A., ... others (2020). Tracking improvement in simulated marine biogeochemistry between cmip5 and cmip6. *Current Climate Change Reports*, *6*(3), 95–119.

Seland, y., Bentsen, M., Oliviè, D. J. L., Toniazzo, T., Gjermundsen, A., Graff, L. S., ... Schulz, M. (2019). *NCC NorESM2-LM model output prepared for CMIP6 CMIP historical [Dataset].* Earth System Grid Federation. Retrieved from https://doi.org/10.22033/ESGF/CMIP6.8036 doi: 10.22033/ESGF/CMIP6.8036

Sutton, A. J., Feely, R. A., Sabine, C. L., McPhaden, M. J., Takahashi, T., Chavez, F. P., ... Mathis, J. T. (2014). Natural variability and anthropogenic change in equatorial pacific surface ocean pco2 and ph. *Global Biogeochemical Cycles*, *28*(2), 131-145. Retrieved from https://agupubs.onlinelibrary.wiley.com/doi/abs/10.1002/2013GB004679 doi: https://doi.org/10.1002/2013GB004679

Swart, N. C., Cole, J. N., Kharin, V. V., Lazare, M., Scinocca, J. F., Gillett, N. P., ... Sigmond, M. (2019a). *CCCma CanESM5-CanOE model output prepared for CMIP6 CMIP historical [Dataset].* Earth System Grid Federation. doi: 10.22033/ESGF/CMIP6.10260

Swart, N. C., Cole, J. N., Kharin, V. V., Lazare, M., Scinocca, J. F., Gillett, N. P.,

... Sigmond, M. (2019b). *CCCma CanESM5 model output prepared for CMIP6 CMIP historical [Dataset].* Earth System Grid Federation. doi: 10.22033/ESGF/CMIP6.3610

Takahashi, T., Olafsson, J., Goddard, J. G., Chipman, D. W., & Sutherland, S. C. (1993). Seasonal variation of co2 and nutrients in the high-latitude surface oceans: A comparative study. *Global Biogeochemical Cycles*, *7*(4), 843-878. Retrieved from https://agupubs.onlinelibrary.wiley.com/doi/abs/10.1029/93GB02263 doi: https://doi.org/10.1029/93GB02263

Takahashi, T., Sutherland, S. C., Sweeney, C., Poisson, A., Metzl, N., Tilbrook, B., ... Nojiri, Y. (2002). Global sea–air co2 flux based on climatological surface ocean pco2, and seasonal biological and temperature effects. *Deep Sea Research Part II: Topical Studies in Oceanography*, *49*(9), 1601-1622. (The Southern Ocean I: Climatic Changes in the Cycle of Carbon in the Southern Ocean) doi: https://doi.org/10.1016/S0967-0645(02)00003-6

Takahashi, T., Sutherland, S. C., Wanninkhof, R., Sweeney, C., Feely, R. A., Chipman, D. W., ... de Baar, H. J. (2009). Climatological mean and decadal change in surface ocean pco2, and net sea–air co_2 flux over the global oceans. *Deep Sea Research Part II: Topical Studies in Oceanography*, *56*(8), 554-577. Retrieved from https://www.sciencedirect.com/science/article/pii/S0967064508004311 (Surface Ocean CO2 Variability and Vulnerabilities) doi: https://doi.org/10.1016/j.dsr2.2008.12.009

Taylor, K. E., Stouffer, R. J., & Meehl, G. A. (2012). An overview of cmip5 and the experiment design. *Bulletin of the American meteorological Society*, *93*(4), 485–498.

Vaittinada Ayar, P., Tjiputra, J., Bopp, L., Christian, J. R., Ilyina, T., Krasting, J. P., ... Yool, A. (2022). Contrasting projection of the enso-driven co_2 flux variability in the equatorial pacific under high warming scenario. *Earth System Dynamics Discussions*, *2022*, 1–31. Retrieved from https://esd.copernicus.org/preprints/esd-2022-12/ doi: 10.5194/esd-2022-12

Wanninkhof, R. (2014). Relationship between wind speed and gas exchange over the ocean revisited. *Limnology and Oceanography: Methods*, *12*(6), 351-362. Retrieved from https://aslopubs.onlinelibrary.wiley.com/doi/abs/10.4319/lom.2014.12.351 doi: https://doi.org/10.4319/lom.2014.12.351

Wieners, K.-H., Giorgetta, M., Jungclaus, J., Reick, C., Esch, M., Bittner, M., ... Roeckner, E. (2019). *MPI-M MPI-ESM1.2-LR model output prepared for CMIP6 CMIP historical [Dataset].* Earth System Grid Federation. doi: 10.22033/ESGF/CMIP6.6595

Yukimoto, S., Koshiro, T., Kawai, H., Oshima, N., Yoshida, K., Urakawa, S., ... Adachi, Y. (2019). *MRI MRI-ESM2.0 model output prepared for CMIP6 CMIP historical [Dataset].* Earth System Grid Federation. doi: 10.22033/ESGF/CMIP6.6842

Ziehn, T., Chamberlain, M., Lenton, A., Law, R., Bodman, R., Dix, M., ... Druken, K. (2019). *CSIRO ACCESS-ESM1.5 model output prepared for CMIP6 CMIP historical [Dataset].* Earth System Grid Federation. doi: 10.22033/ESGF/CMIP6.4272

Zuo, H., Balmaseda, M. A., Tietsche, S., Mogensen, K., & Mayer, M. (2019). The ecmwf operational ensemble reanalysis–analysis system for ocean and sea ice: a description of the system and assessment. *Ocean Science*, *15*(3), 779–808. Retrieved from https://os.copernicus.org/articles/15/779/2019/ doi: 10.5194/os-15-779-2019